AGU PUBLICATIONS

Space Weather

RESEARCH ARTICLE
10.1002/2016SW001506

Electron flux models for different energies at geostationary orbit

R. J. Boynton[1], M. A. Balikhin[1], D. G. Sibeck[2], S. N. Walker[1], S. A. Billings[1], and N. Ganushkina[3,4]

[1]Department of Automatic Control and Systems Engineering, University of Sheffield, Sheffield, UK, [2]NASA Goddard Space Flight Center, Greenbelt, Maryland, USA, [3]Finnish Meteorological Institute, Helsinki, Finland, [4]University of Michigan, Ann Arbor, Michigan, USA

Key Points:
- A set of electron flux forecast models is deduced for energy ranges sampled by GOES 13
- The deduced models forecasting performance statistics are detailed
- The models will be implemented as a real-time forecasting tool

Correspondence to:
R. J. Boynton,
rboynton85@gmail.com

Citation:
Boynton, R. J., M. A. Balikhin, D. G. Sibeck, S. N. Walker, S. A. Billings, and N. Ganushkina (2016), Electron flux models for different energies at geostationary orbit, *Space Weather*, *14*, 846–860, doi:10.1002/2016SW001506.

Received 15 AUG 2016
Accepted 9 OCT 2016
Accepted article online 14 OCT 2016
Published online 26 OCT 2016

Abstract Forecast models were derived for energetic electrons at all energy ranges sampled by the third-generation Geostationary Operational Environmental Satellites (GOES). These models were based on Multi-Input Single-Output Nonlinear Autoregressive Moving Average with Exogenous inputs methodologies. The model inputs include the solar wind velocity, density and pressure, the fraction of time that the interplanetary magnetic field (IMF) was southward, the IMF contribution of a solar wind-magnetosphere coupling function proposed by Boynton et al. (2011b), and the *Dst* index. As such, this study has deduced five new 1 h resolution models for the low-energy electrons measured by GOES (30–50 keV, 50–100 keV, 100–200 keV, 200–350 keV, and 350–600 keV) and extended the existing >800 keV and >2 MeV Geostationary Earth Orbit electron fluxes models to forecast at a 1 h resolution. All of these models were shown to provide accurate forecasts, with prediction efficiencies ranging between 66.9% and 82.3%.

1. Introduction

The radiation belts consist of energetic particles trapped by the terrestrial magnetic field and were discovered from the first in situ space radiation measurements. The outer radiation belt is made up of trapped electrons ranging in energy from keVs to several MeVs. *Blake et al.* [1992] and *Reeves* [1998] showed that the electron fluxes can vary by several orders of magnitude in a few hours. The high fluence of these energetic electrons can cause a number of problems on spacecraft depending on the electron energy. For example, low-energy electrons (1 keV to 100 keV) can cause surface charging that interferes with the satellite electronic systems [*Olsen*, 1983; *Mullen et al.*, 1986], while higher energies (above 1 MeV and above) cause deep dielectric charging that may permanently damage the materials on board the satellite [*Baker et al.*, 1987; *Wrenn et al.*, 2002; *Gubby and Evans*, 2002; *Lohmeyer and Cahoy*, 2013; *Lohmeyer et al.*, 2015].

There are still many unanswered questions about the mechanisms involved within the radiation belts, such as the acceleration mechanisms and loss processes of the electrons [*Friedel et al.*, 2002]. Since we do not have a complete understanding of the physics, radiation belt models based on first principals struggle to capture the variable dynamics of the system [*Horne et al.*, 2013b]. As such, these models often exhibit large errors between the forecast and the observed electron population [*Horne et al.*, 2013a].

The system identification approach has also been applied to modeling the radiation belts. In this approach, models are automatically deduced from input-output data by the system identification algorithms. The system identification methodologies include linear prediction filters [*Baker et al.*, 1990], dynamic linear models [*Osthus et al.*, 2014], neural networks [*Koons and Gorney*, 1991; *Freeman et al.*, 1998; *Ling et al.*, 2010], and Nonlinear Autoregressive Moving Average with Exogenous inputs (NARMAX) [*Wei et al.*, 2011; *Boynton et al.*, 2013a, 2015]. While linear prediction filters and dynamic linear models are suitable for linear systems, the main advantage of NARMAX and neural networks is that they are capable of modeling nonlinear dynamics within the system. NARMAX and neural networks can both provide accurate and reliable models for nonlinear systems such as the radiation belts; however, NARMAX has the advantage of interpretability over neural networks. Neural networks result in the relationship between input and output measurements being described through a maze of multilayered neurones, in which each connection has an associated weight factor and each neurone has an activation function. This makes neural networks extremely difficult to interpret, i.e., to find out how the input variables couple together to produce changes in the output. In contrast, NARMAX models can result in a simple polynomial, from which understanding how the inputs change the output is intuitive.

Therefore, this study uses the NARMAX methodologies to model the electron fluxes observed by the Geostationary Operational Environmental Satellites (GOES), situated in Geostationary Earth Orbit (GEO).

The main aim of this study is to create reliable forecast models for the electron flux energy ranges observed by the third-generation GOES. The second aim is to increase temporal resolution of the forecast to that which currently operates on the University of Sheffield Space Weather Website (http://www.ssg.group.shef.ac.uk/USSW/UOSSW.html) and was developed by *Boynton et al.* [2015]. In section 2, we discuss the methodology used to deduce the forecast models. This includes a brief description of the NARMAX algorithm. Section 3 presents an extension of the current 24 h resolution >800 keV and >2 MeV GEO electron flux models, developed by *Boynton et al.* [2015], to 1 h resolution and a calculation of their performance. In section 4, the methodology and data used to derive the low-energy models and the results of the model performances are shown. The limitations of the models and their performance are discussed in section 5, and the conclusions from this study are presented in section 6.

2. NARMAX Methodology

As stated in section 1, NARMAX models provide reliable forecasts and are also easy to interpret. As such, the methodology has been applied to a wide range of scientific fields, from analyzing the adaptive changes in the photoreceptors of *Drosophila* flies [*Friederich et al.*, 2009] to modeling the tide at the Venice Lagoon [*Wei and Billings*, 2006]. In the field of space physics, the methodology was first used to model the *Dst* index using the half-wave rectifier (solar wind velocity multiplied by the southward interplanetary magnetic field (IMF) component) as the input [*Balikhin et al.*, 2001; *Boaghe et al.*, 2001]. More recently, due to lack of knowledge about the inputs to the *Dst* index system, *Boynton et al.* [2011b] used the NARMAX model structure detection methodology to identify the main control parameter, or solar wind coupling function, for geomagnetic storms quantified using the *Dst* index. This coupling function was $p^{1/2}V^{4/3}B_T \sin^6(\theta/2)$, where p is the pressure, V is the velocity, $B_T = \sqrt{(B_y^2+B_z^2)}$ is the tangential IMF, and $\theta = \tan^{-1}(B_y/B_z)$ is the clock angle of the IMF in GSM coordinates. *Boynton et al.* [2011a] used this coupling function to deduce a reliable model for the *Dst* index. *Boynton et al.* [2013b] and *Balikhin et al.* [2011] employed a similar approach to identify the solar wind control parameters for electron fluxes at GEO. In these studies, they found that the solar wind velocity and density were the main control parameters. The interpretability of these results allowed *Balikhin et al.* [2012] to make a direct comparison with the energy diffusion equation, where they found that acceleration due to local diffusion does not dominate at GEO. Recently, the NARMAX model structure detection methodology has been employed by *Beharrell and Honary* [2016] to determine the relationship between the solar wind and *SYM-H*.

NARMAX models were first proposed by *Leontaritis and Billings* [1985a, 1985b] who demonstrated that the models have the potential to represent a wide class of nonlinear systems. A Multi-Input Single-Output NARMAX model, which was used in this study to model the electron fluxes at GEO, is expressed by

$$\begin{aligned} y(t) = F\big[&y(t-1),\ldots,y\left(t-n_y\right),\\ &u_1(t-1),\ldots,u_1\left(t-n_{u_1}\right),\ldots,\\ &u_m(t-1),\ldots,u_m\left(t-n_{u_m}\right),\ldots,\\ &e(t-1),\ldots,e\left(t-n_e\right)\big]+e(t) \end{aligned} \tag{1}$$

where y, u, and e represent the output, input, and error terms, respectively, $F[\cdot]$ represents some nonlinear function (a polynomial in the case of this study), m is the number of system inputs, and $n_y, n_{u_1}, \ldots, n_{u_m}, n_e$ are the maximum time lags for the output, each of the m inputs, and the error, respectively.

Billings et al. [1988] developed the first Forward Regression Orthogonal Least Squares (FROLS) algorithm that automatically fits a NARMAX model using input-output training data sets. Simply put, the overall algorithm developed by *Billings et al.* [1988] involved three stages. The first stage is model structure detection, which identifies the variables or combination of variables that control the evolution of the system. In equation (1), the expansion of $F[\cdot]$ in terms of a high-degree polynomial results in a huge number of monomials, especially if there are many possible inputs. The vast majority of the possible monomials will have little influence on the system; i.e., the coefficients of the monomial will be zero. Therefore, only a small number of monomials are required to represent the dynamics of the system. The FROLS procedure identifies the most significant monomials by use of the Error Reduction Ratio (ERR). Once the model structure is detected, the second stage is to estimate the coefficient for each of the monomials detected in the model. These first two stages are

referred to as training the model. The final stage is to validate the model. Since its inception, many variants on the FROLS algorithm have been developed [*Billings et al.*, 1989; *Mao and Billings*, 1997; *Wei and Billings*, 2008]. This study employs the Iterative Orthogonal Forward Regression (IOFR) algorithm, developed by *Guo et al.* [2014], which is more likely to detect the optimal model when the data are oversampled.

The IOFR is largely based upon the initial FROLS algorithm, where the ERR of each of the monomials is calculated with respect to the output. The monomial with the highest ERR is then selected as the first monomial for the initial model structure. For the next step of the algorithm, all other monomials are orthogonalized relative to the first monomial that has just been selected. This effectively removes the first monomials contribution to the output from the remaining monomials. The ERRs of these orthogonalized monomials are then calculated with respect to the output, and the one with the highest ERR is selected as the second monomial for the initial model. For the third step, the remaining monomials are orthogonalized relative to both the first and second monomials selected for the initial model and the ERR is calculated. Again, the orthogonalized monomial with the highest ERR is selected and this will be the third monomial for the model. This process of orthogonalizing the remaining monomials with respect to all the selected model terms then selecting the orthogonalized monomial with the highest ERR for the model is continued until the model has the optimum number of model monomials. To decide the optimum number of model terms, this study employed the Adjustable Prediction Error Sum of Squares (APRESS) [*Billings and Wei*, 2008]. After each monomial is selected during every step of the FROLS algorithm, the APRESS is calculated from the ERR

$$\mathrm{APRESS} = \frac{1}{(1-\lambda k/N)^2}\left(1-\sum_{i=1}^{k}\mathrm{ERR}_i\right) \tag{2}$$

where N is the number of data points, k is the number of monomials that has been selected, and λ is an adjustable factor that was between 5 and 10. At each step, i, APRESS(i) is calculated and compared to the previous APRESS($i-1$). APRESS will decrease as each significant monomial is added to the model until a local minima is reached. After this turning point, the addition of more model monomials is less likely to increase the performance of the model and may lead to the model becoming overfit [*Billings and Wei*, 2008]. Therefore, the turning point in APRESS dictates the optimum number of model monomials and the initial model polynomial structure is obtained. A least squares procedure then identifies the coefficients for each monomial to yield the model.

3. Increasing the Time Resolution of the Existing >800 keV and >2 MeV GEO Electron Flux Models

Models for forecasting the fluxes of >800 keV and >2 MeV electrons at GEO were developed by *Boynton et al.* [2015]. These models were deduced using the NARMAX methodology and provide a 1 day resolution forecast for 1 day ahead. Both of these models were shown to have a high prediction efficiency for estimating the next day's electron flux value [*Boynton et al.*, 2015]. The forecast results can be found online at www.ssg.group.shef.ac.uk/USSW/UOSSW.html.

The original model only produces one forecast for the day. This forecast is for the average electron flux between 00:01 UTC 1 day to 00:00 UTC on the next day, calculated at 00:01 UTC. This means that at the start of every UTC day the original model calculates a forecast for the average electron flux over the next 24 h. One of the aims of this study is to increase the temporal resolution of these forecasts. Therefore, the time resolution of the >800 keV and >2 MeV GEO electron flux models was extended to give a forecast of the electron fluxes every hour for the next 24 h in contrast to only one daily forecast per day. This means that every hour the model will calculate a forecast for the average electron flux over the next 24 h, producing 24 forecasts per day.

3.1. Data and Methodology

The >800 keV and >2 MeV electron flux models rely on solar wind inputs to forecast the electron flux. The solar wind inputs are the daily average velocity and density and the amount of time the IMF is southward in a 24 h period. The 1 min solar wind velocity, density, and IMF B_z component data were obtained from the OMNI website (http://omniweb.gsfc.nasa.gov/ow_min.html) from 1 January 2011 to 28 February 2015. At every hour, the past 24 h average of the solar wind velocity and density was calculated. For example, the point at 10:00:00 UTC on 5 January 2015 is an average of the 1440 1 min points between 10:01:00 UTC on

4 January 2015 and 10:00:00 UTC on 5 January 2015. In addition, the number of minutes that the IMF was southward during the past 24 h was determined for the final input.

The electron flux data used to analyze the performance of the extended temporal resolution >800 keV and >2 MeV GEO electron flux models were from GOES 13. The electron fluxes on board the GOES 13 satellite are measured by the Energetic Proton Electron and Alpha Detector (EPEAD) [*Hanser*, 2011] and the Magnetospheric Electron Detector (MAGED). [*Hanser*, 2011]. The data for these instruments can be accessed from http://www.ngdc.noaa.gov/stp/satellite/goes/dataaccess.html, and the MAGED will be discussed in section 4.1.

The EPEAD measures the relativistic integral electron fluxes and has two detectors pointing in opposite directions, both tangential to the spacecrafts orbit, named the east and west detectors. Since the EPEAD measures integral flux, the >2 MeV electrons will be measured by the >800 keV channel; however, the >2 MeV electrons account for less than 3% of the electrons detected on average. These data were used to assess the 1 h temporal resolution of the SNB^{3}GEO electron flux models (SN stands for Sheffield NARMAX, and B^3 corresponds to the letters of surnames of three model developers and GEO stands for geostationary orbit). The data period used for this part of the study was from 1 January 2011 to 28 February 2015. The study employed the >800 keV and >2 MeV energy channels from both the east and west detectors on board the GOES 13 satellite. The 5 min proton-corrected electron flux values were averaged between the east and west detectors. This was then time averaged resulting in a data set with 1 h resolution, such that each 1 h point was determined by averaging the 5 min data over the past 24 h; e.g., the point at 10:00:00 UTC on 5 January 2015 is average of the 288 5 min points between 10:05:00 UTC on 4 January 2015 and 10:00:00 UTC on 5 January 2015. These data were then compared to the model forecast. The 1 h moving average data will allow for a more continuous forecast of the daily average electron flux, such that every hour the online model will be able to forecast the electron flux value over the next 24 h, compared to only producing one forecast for each UTC day. Therefore, the forecast horizon for both the >800 keV and >2 MeV models will be 24 h.

3.2. Model Performance

The >800 keV and >2 MeV GEO electron flux models were run using the 1 h resolution input data, and the results were compared to the EPEAD 1 h electron flux data, for the period from 1 January 2011 to 28 February 2015. The performance of the models during the period could then be analyzed.

The performance of the models was assessed statistically by the correlation coefficient (CC), equation (3), and the prediction efficiency (PE), equation (4), which are commonly used to assess models [*Temerin and Li*, 2006; *Li*, 2004; *Boynton et al.*, 2011a; *Wei et al.*, 2004; *Boynton et al.*, 2015; *Rastatter et al.*, 2013].

$$\rho_{y\hat{y}} = \frac{\sum_{t=1}^{N}\left[(y(t)-\bar{y})\left(\hat{y}(t)-\bar{\hat{y}}\right)\right]}{\sqrt{\sum_{t=1}^{N}\left[(y(t)-\bar{y})^2\right]\sum_{t=1}^{N}\left[\left(\hat{y}(t)-\bar{\hat{y}}\right)^2\right]}}100\% \tag{3}$$

$$E_{\mathrm{PE}} = \left[1 - \frac{\sum_{t=1}^{N}\left[\left(y(t)-\hat{y}(t)\right)^2\right]}{\sum_{t=1}^{N}\left[(y(t)-\bar{y})^2\right]}\right]100\% \tag{4}$$

Here E_{PE} is the PE, ρ is the CC, $y(t)$ is the output at time t, $\hat{y}$ is the estimated output from the model, N is the length of the data, and the bar signifies the average.

3.2.1. The >800 keV Model

Figure 1a shows the past 24 h average >800 keV electron flux measured by GOES in blue and the model 24 h ahead forecast in orange for the period from 1 January 2011 to 28 February 2015, while Figure 1b depicts the model error ($e = \log_{10}(J_{\mathrm{GOES}}) - \log_{10}(J_{\mathrm{model}})$). During this period, the PE was 72.1% and the CC was 85.1%.

3.2.2. The >2 MeV Model

Figure 1c shows the past 24 h average >2 MeV electron flux measured by GOES in blue and the model 24 h ahead forecast in orange for the period from 1 January 2011 to 28 February 2015, Figure 1d depicts the >2 MeV electron flux model error. The PE for the >2 MeV model was 82.3%, while the CC was 90.9%. Figures 1a and 1c reflect the better statistical performance of the >2 MeV model over the >800 keV model, since it can clearly be seen that the >2 MeV model follows more closely the blue observed GOES electron flux, particularly for the lower electron flux values.

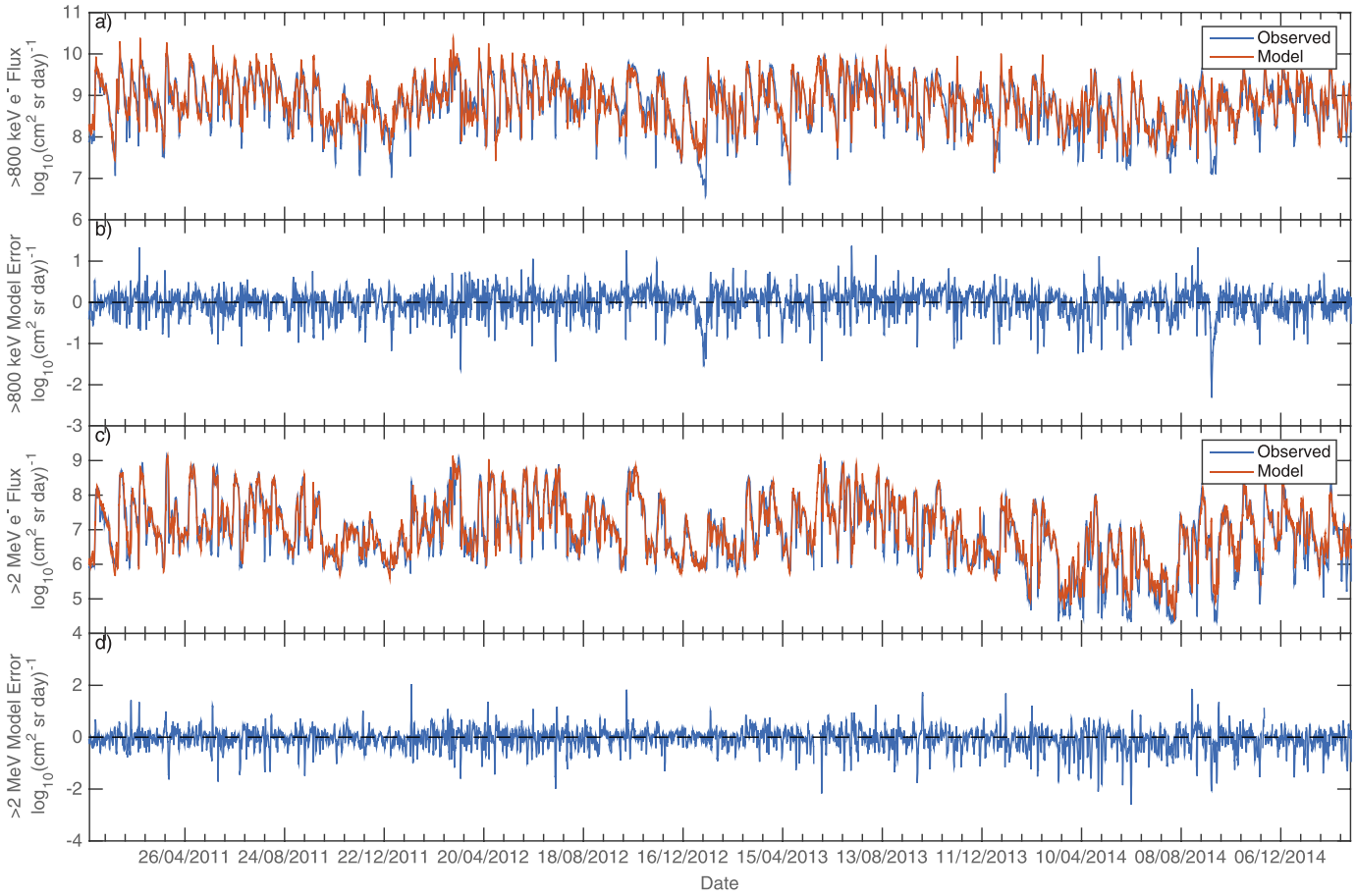

Figure 1. (a) The past 24 h average >800 keV electron flux measured by GOES in blue and the model 24 h ahead forecast in orange for the period from 1 January 2011 to 28 February 2015. (b) The >800 keV electron flux model error ($\log_{10}(J_{GOES}) - \log_{10}(J_{model})$). (c) The past 24 h average >2 MeV electron flux measured by GOES in blue and the model 24 h ahead forecast in orange for the period from 1 January 2011 to 28 February 2015. (d) The >2 MeV electron flux model error ($\log_{10}(J_{GOES}) - \log_{10}(J_{model})$).

4. Modeling the Low-Energy Electron Fluxes Measured by GOES 13

Models to forecast the low-energy electrons measured by GOES satellites were deduced using the NARMAX IOFR algorithm. This method requires input-output data for training the models.

4.1. Data and Methodology

The electron flux data for the training and validation of these models come again from GOES 13. The MAGED has nine telescopes pointing in different directions and measures the lower energy differential electron fluxes in five energy channels: 30–50 keV, 50–100 keV, 100–200 keV, 200–350 keV, and 350–600 keV [*Hanser*, 2011]. The data period used for this part of the study was from 1 May 2010 to 28 February 2015 and employed all energy channels available from the instrument. This study is concerned mainly with the trapped electrons and therefore should not use a telescope that is directed in the loss cone, which is <5° at GEO. Since telescopes 1–5 of the MAGED are in the east-west plane, they should be directed farther away from the loss cone than telescopes 6–9, which are directed north or south. Figure 2a shows the 30–50 keV electron flux for the nine telescopes, and Figure 2b shows the pitch angle for each of the telescopes, which can be downloaded from http://www.ngdc.noaa.gov/stp/satellite/goes/dataaccess.html. These are displayed for an arbitrary period between 13 November 2012 and 27 October 2013. The figure shows that telescopes 1–6 have pitch angles between ~110° and ~40°, and with a telescope cone angle of 30° none of these should be directed in the loss cone. Since GOES 13 is positioned above the equator at ~0° latitude and the magnetic North Pole is ~60° west of the satellite and has a latitude of ~85° north during this period, the telescope pointing farthest south (telescope 7) is the only one permanently looking in the loss cone. As such, the electron flux of telescope 7 is less than the others. Therefore, we arbitrarily chose the data from telescope 3 to use as the output for this

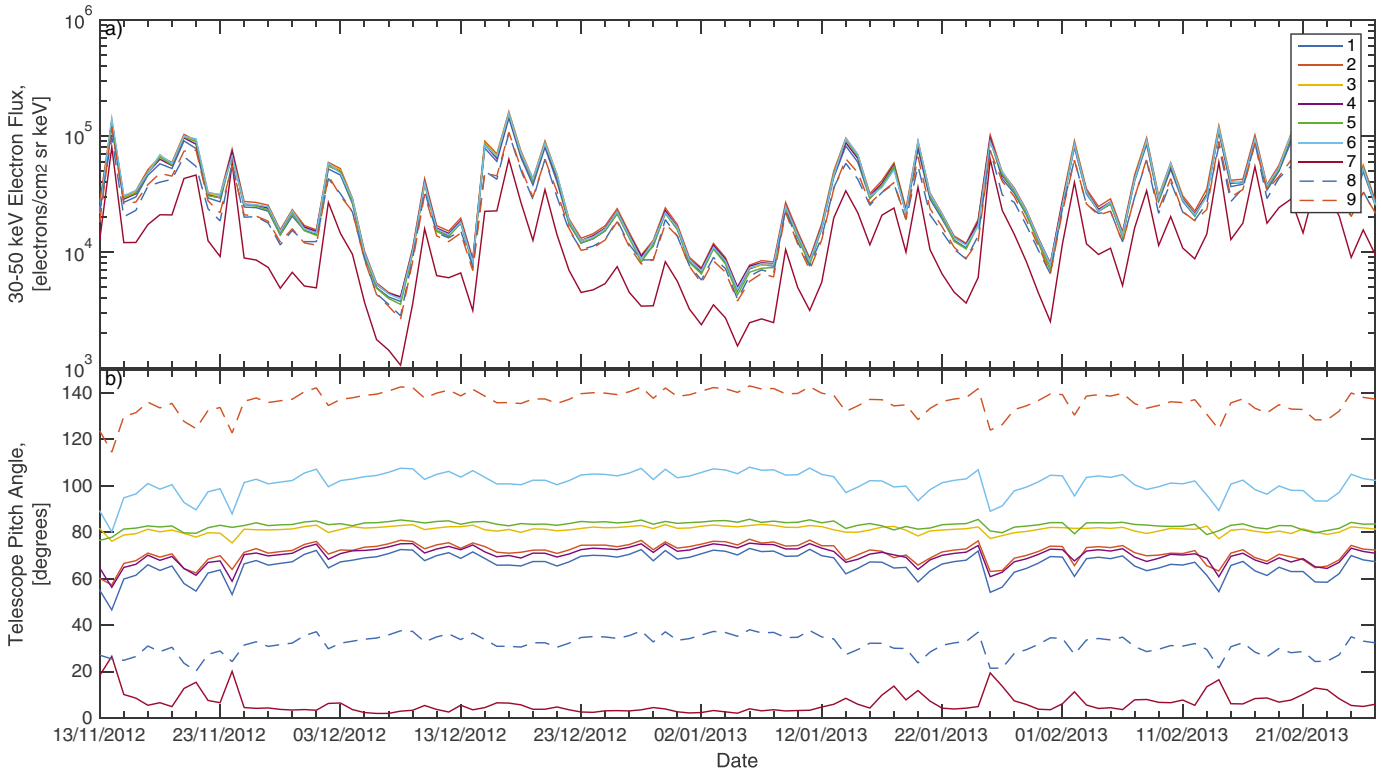

Figure 2. (a) The 30–50 keV electron flux for the nine telescopes. (b) The pitch angle of each telescope. For the period from 13 November 2012 to 27 February 2013.

particular study. Using only one telescope makes the real-time online procedure of processing the data more simple, which will reduce the possibility of bugs occurring thus making the real-time procedure more reliable.

Solar wind and geomagnetic indices were used as input data for training the models. The 1 min solar wind velocity, density, and IMF data were obtained from the OMNI website (http://omniweb.gsfc.nasa.gov/ow_min.html), while the *Dst* geomagnetic index was from the World Data Center for Geomagnetism, Kyoto (http://wdc.kugi.kyoto-u.ac.jp/index.html).

4.2. Model Training

The training data were from 1 March 2011 to 28 February 2013. For the training data, the 1 min corrected electron flux values were daily averaged between 00:01:00 UTC and 00:00:00 UTC the next day for each day, resulting in training 790 data points. This was chosen because a NARMAX model requires a training set that covers a wide range of the systems variation, which is usually approximately a few hundred data points [*Billings et al.*, 1989].

The studies by *Boynton et al.* [2013b] and *Balikhin et al.* [2012] showed that the time delay in the reaction of electron fluxes to changes in the solar wind increases with the energy. The high-energy models of >800 keV and >2 MeV had minimum time delays of 1 day, and thus, it is possible to forecast 1 day into the future. However, same day values of the solar wind affect the current low-energy electron flux. Therefore, it is not possible to forecast 1 day ahead. To get around this problem, the past 24 h averages were calculated for each hour, as previously described. Therefore, the input time lags in the algorithm, n_{u_m}, were shifted hourly not daily. For example, if input $U(t-10\text{ h})$ is selected by the model, this monomial represents the average of the points between $U(t-10\text{ h})$ and $U(t-34\text{ h})$. Initially, a number of window intervals from 1 h averages, past 3 h, past 12 h, and 24 h were investigated. The 12 and 24 h windows gave the better results, but it was decided to use 24 h averaging for convenience because the same inputs could be used for >2 MeV and 800 keV models. This also makes the procedure simpler when implemented online and therefore less chance of bugs.

The algorithm was run for the five energy ranges using lagged inputs from 2 to 48 h. These inputs were the solar wind velocity V and density n, the amount of time the IMF is southward in a 24 h period T_{Bs}, the *Dst* index, and the term resulting from the coupling function proposed by *Balikhin et al.* [2010] and

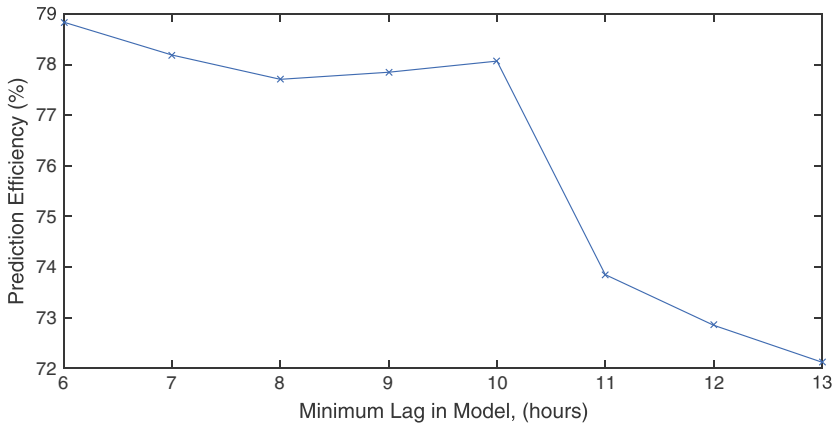

Figure 3. The PE of a 30–50 keV model between 1 May 2010 and 28 February 2011 versus the minimum lag included in that model.

Boynton et al. [2011b], $B_T \sin^6(\theta/2)$ (where $B_T = \sqrt{(B_y^2 + B_z^2)}$ is the tangential IMF and $\theta = \tan^{-1}(B_y/B_z)$ is the clock angle of the IMF). Therefore, the NARXAX model of the electron flux J will be

$$\begin{aligned} J(t) = F[&J(t-24), J(t-48), \\ &V(t-2), V(t-3), \ldots, V(t-48), \\ &n(t-2), n(t-3), \ldots, n(t-48), \\ &T_{Bs}(t-2), T_{Bs}(t-3), \ldots, T_{Bs}(t-48), \\ &Dst(t-2), Dst(t-3), \ldots, Dst(t-48), \ldots, \\ &B_T \sin^6(\theta/2)(t-2), B_T \sin^6(\theta/2)(t-3), \ldots, B_T \sin^6(\theta/2)(t-48), \\ &e(t-24), e(t-48)] + e(t) \end{aligned} \tag{5}$$

where the lags are in hours. When F is expanded to a second degree polynomial, there will be over 10,000 monomials for the FROLS algorithm to search through.

For the 30–50 keV electrons, a compromise had to be made between producing a reliable forecast and the forecast horizon, the amount of time the model can forecast into the future. The model detected by the algorithm included input terms I, with a minimum lag of 6 h $J(t) = F[I(t-6), \ldots]$. Therefore, employing the inputs at the present time t, it is possible to estimate the electron flux 6 h into the future, $J(t+6) = F[I(t), \ldots]$. To increase the forecast horizon, the ≤6 h time lagged monomials were manually removed from the algorithms search to see if the performance of the model, based on PE and the CC, dropped significantly on a period of test data from 1 May 2010 to 28 February 2011. It was found that there was only a negligible drop in performance if the detected model had input terms with a minimum of 7 h time lag. This process of manually removing monomials with larger and larger time lags was continued until there was a significant performance drop in the model output. Figure 3 shows the results of this process with PE having a significant drop at a minimum lag of 11 h. Therefore, the model with a minimum of 10 h lag was selected as the final 30–50 keV model and could forecast the past 24 h average of the flux 10 h in the future. This methodology was repeated for the other four

Table 1. Table Showing the Performance of the Five Low-Energy Electron Flux Models As Well As the Forecast Length

Model	Forecast Horizon	1 Day PE (%)	1 Day CC (%)	1 h PE (%)	1 h CC (%)
30–50 keV	10 h	72.0	84.9	66.9	82.0
50–100 keV	12 h	70.7	84.2	69.2	83.5
100–200 keV	16 h	71.1	84.4	73.2	85.6
200–350 keV	24 h	69.5	83.7	71.6	84.9
350–600 keV	24 h	69.9	83.8	73.6	85.9

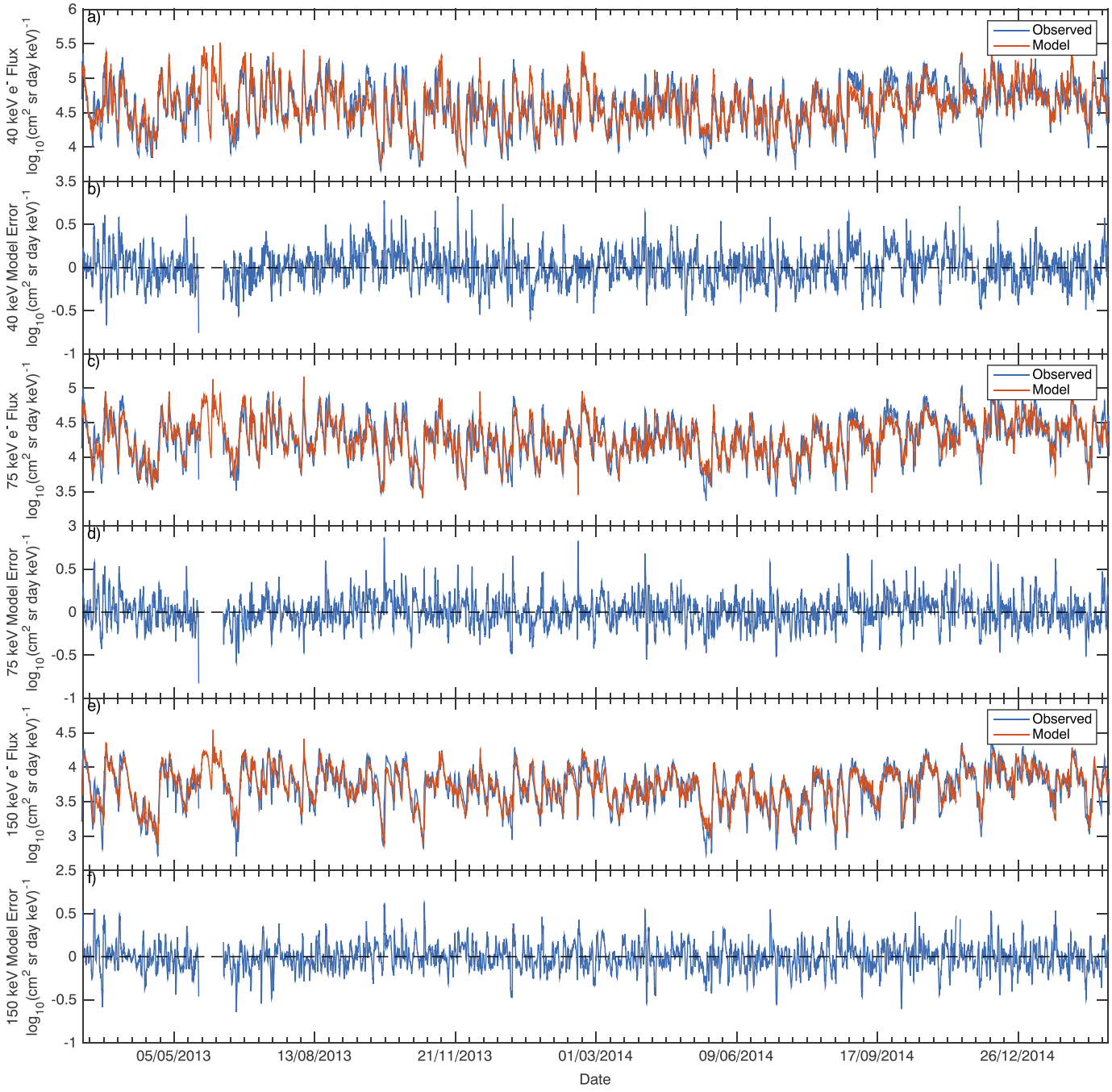

Figure 4. The daily average (a) 30–50 keV, (c) 50–100 keV, and (e) 100–200 keV electron flux measured by GOES in blue and the model forecast in orange for the period from 1 March 2013 to 28 February 2015 and (b) 30–50 keV, (d) 50–100 keV, and (f) 100–200 keV model error ($\log_{10}(J_{GOES}) - \log_{10}(J_{model})$).

energy channels, and as with the studies by *Boynton et al.* [2013b] and *Balikhin et al.* [2012], the time delay of electron fluxes increased with the energy. The forecast horizons for each of the models are shown in Table 1. In each of the NARMAX models, the monomial with the minimum lag is due to a velocity component within the monomial. For example, in the 30–50 keV model, the FROLS algorithm selected $V(t-10)B_T \sin(\theta/2)(t-12)$ as the exogenous monomial with the highest ERR. The exogenous monomial with the highest ERR in each of the models had a component of the velocity at the models minimum lag. For the three lowest energies the velocity was coupled with the IMF factor, while for the two higher energies the FROLS algorithm selected the linear velocity.

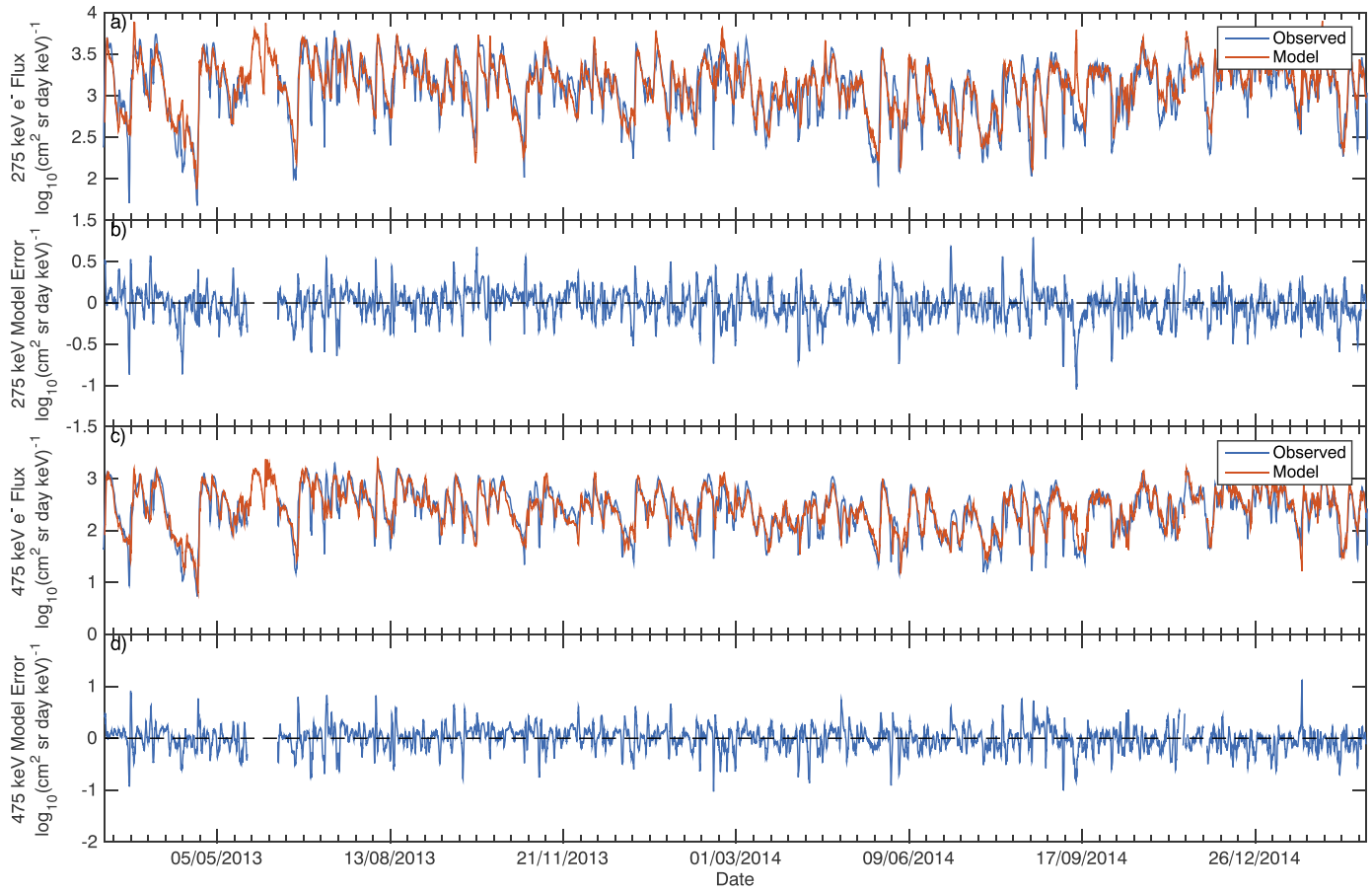

Figure 5. The daily average (a) 200–350 keV and (c) 350–600 keV electron flux measured by GOES in blue and the model 24 h ahead forecast in orange for the period from 1 March 2013 to 28 February 2015 and (b) 200–350 keV and (d) 350–600 keV model error ($\log_{10}(J_{GOES}) - \log_{10}(J_{model})$).

4.3. Final Model Performance

The performance of the models was analyzed statistically using the PE and CC. Each of the models were run on the data from 1 March 2013 to 28 February 2015. At first, the models were run on the daily averaged data which resulted in 730 points for the period. Then, the models were extended to 1 h resolution of the past 24 h average, which contains 17,520 points, to assess each of the model's performance with an increased time resolution.

Table 1 lists the performance of the five low-energy electron flux models, showing the PE and CC for the 1 day and 1 h resolution data. The table also shows the minimum time lag used in the model and thus how far ahead the model can forecast into the future. This is in agreement with the studies by *Boynton et al.* [2013b] and *Balikhin et al.* [2012], since the minimum time lags increase with energy. The PEs of the models are between 66.9% and 73.6%, which means that the mean square error is well within the variance of the fluxes, and the CC 82% and 85.9%. The results of the five models for the 1 h resolution data are illustrated in Figures 4a (30–50 keV model), 4(c) (50–75 keV model), 4e (100–200 keV model), 5a (200–350 keV model), and 5c (350–600 keV model). These figures show the observed GOES electron flux in blue and the model forecast in orange. Below each of these figures are their respective model error plots in blue, where the dashed black line is zero error. The figures show that the models approximately follow the measured fluxes with the errors within 1 order of magnitude.

5. Discussion

One of the aims of this study was to increase the time resolution of the forecasts of the >800 keV and >2 MeV GEO electron flux models that currently operate online. These models provide daily averaged 1 day ahead forecasts for each UTC day. Increasing the resolution of the model by using 1 h averages of the GOES data is not

that simple because during a 24 h GEO orbit there is a significant spatial variation of the electron fluxes that is independent of any temporal changes due to adiabatic acceleration and loss. This is due to changes in the structure of the terrestrial magnetic field, where the compressed dayside leads to an increase in the strength of the magnetic field compared to the nightside. As electrons drift from the nightside to the dayside, these changes in the structure of the magnetic field cause the electrons to move outward as they approach noon and back inward as they drift back to midnight. Since the electron flux is generally greater deeper within the magnetosphere, higher fluxes are observed when GOES is situated at noon compared to midnight. This spatial variation makes it difficult to deduce a data-based model because the satellites position is always changing. As such, to achieve the aim of increasing the temporal resolution, we employed a moving average of the preceding 24 h calculated every hour. We applied the existing >800 keV and >2 MeV GEO electron flux models to this 1 h averaged data because these models have already been proven to be reliable in their online operation [*Balikhin et al.*, 2016]. This change in input time resolution resulted in high values for the PE and CC, higher than those reported by *Boynton et al.* [2015]. *Boynton et al.* [2015] showed, using the 1 day resolution data, that the >2 MeV model had a PE of 78.6% and a CC of 89.4% and that the >800 keV model had a PE of 70% and a CC of 84.7% between the 1 January 2011 and 30 June 2012, all of which are lower than the results shown in this study. However, these statistics should really be compared over the same time period. Based on the time period between the 1 January 2011 and 30 June 2012, the 1 h PE was 76.0% and the CC was 87.5% for the >800 keV model and the PE was 82.3% and the CC was 90.8% for the >2 MeV model. Therefore, these models perform better using the 1 h resolution data. It can be seen that the >2 MeV model has a higher PE and CC than the >800 keV model for all the periods of data. One of the explanations for this could be that since it takes more time for the electrons to be accelerated to >2 MeV, this larger time delay may allow for a more accurate prediction. Another explanation is that the variance of the GOES logarithmic >2 MeV fluxes was over twice that of the logarithmic >800 keV fluxes for this time period and since prediction efficiency is dependent on the variance of the observed signal, a larger variance for the same mean squared error will mean a higher prediction efficiency. Three out of the five lower energy models also performed better using the 1 h resolution data, where only the two lowest energy models had lower performance statistics on the 1 h resolution data compared to the 1 day resolution data.

One of the limitations of the three lowest energy electron models is that the advance time of the forecast is less than the higher-energy models, since the low-energy electron fluxes at GEO respond to solar wind changes significantly faster than high-energy electrons [*Balikhin et al.*, 2012; *Boynton et al.*, 2013b]. The 30–50 keV model is only able to forecast the 24 h average electron flux 10 h into the future, which means that 14 h of this average is already measured. Also, it should be noted that better models with higher performance statistics for the MAGED models, except for the 350–600 keV energy channel, could be obtained if the forecast length was sacrificed. For example, the 30–50 keV model had a 4% higher PE if 6 h time lags were included in the algorithm but this would mean that 18 h of the forecast had already been measured by GOES.

The distributions of the model errors ($\log_{10}(J_{GOES}) - \log_{10}(J_{model})$) were plotted to provide some technical information about the quality of the models. Moreover, the distribution of model errors when the *Dst* index <−40 nT was also plotted to show the model performance during geomagnetic activity. Figure 6 shows the distributions for the MAGED energies, while Figure 7 shows the distributions for the EPS energies. The variance of the model errors, σ_e, is also shown in the top right distributions. The distribution of the model errors for all energies resembles a normal distribution. For the EPEAD energy models, the distribution of the errors is wider, which could be due to the larger variance of the integral fluxes. From the channels between 200 and 350 keV to >2 MeV (Figures 6g, 6i, 7a, and 7c), it can be seen that more errors occur <−0.5 than >0.5. The errors <−0.5 indicate that the model prediction was higher than the GOES observation. This could be due to the model overshooting or missing electron flux dropouts. When inspecting the model error distribution during geomagnetically active times, the trend of more negative errors occurring can be seen down to the 100–200 keV (Figures 6f, 6h, 6j, 7b, and 7d). This implies that these models tend to overshoot or miss dropouts during geomagnetic storms.

To investigate whether the model is tending to overshoot or miss dropouts, the model output versus observed values were plotted for 1 month time scales along with the *Dst* index. Figure 8 shows the observed electron flux in blue with the model forecast in orange for the various energy channels (Figures 8a–8g) and the *Dst* index (Figure 8h) between 15 April 2013 and 15 May 2013. The figure shows that a moderate geomagnetic storm occurs on 24 April with a *Dst* index of ∼−50 nT, which results in the enhancement of the electron fluxes for all energy ranges, with the lower energies reacting on the same day as the main phase of the storm and the

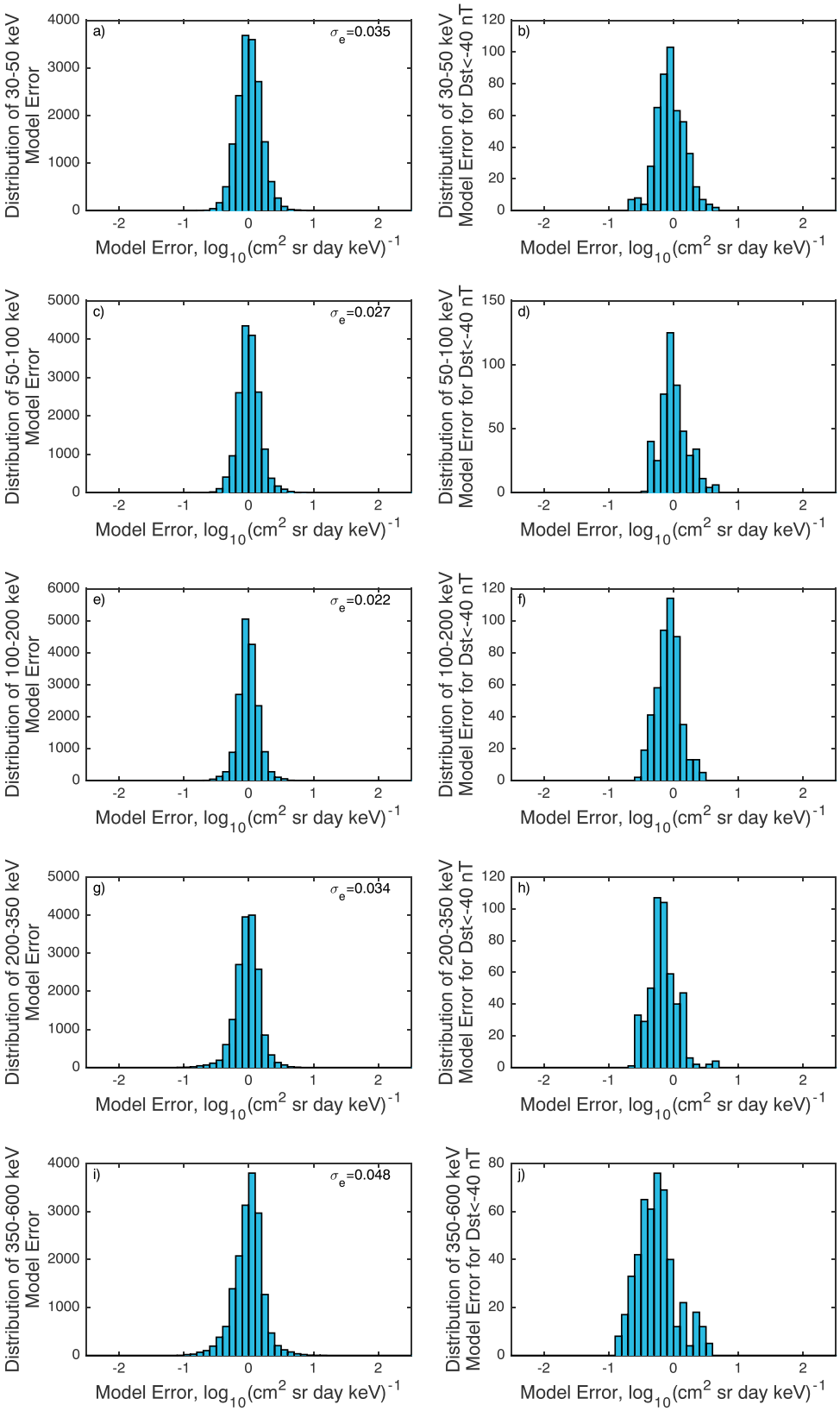

Figure 6. (a, c, e, g, and i) Distribution of the model errors ($\log_{10}(J_{GOES}) - \log_{10}(J_{model})$) for the MAGED energy channels with the variance of the model errors, σ_e, shown in the top right of each panel. (b, d, f, h, and j) Distribution of the model errors when $Dst < -40$ nT.

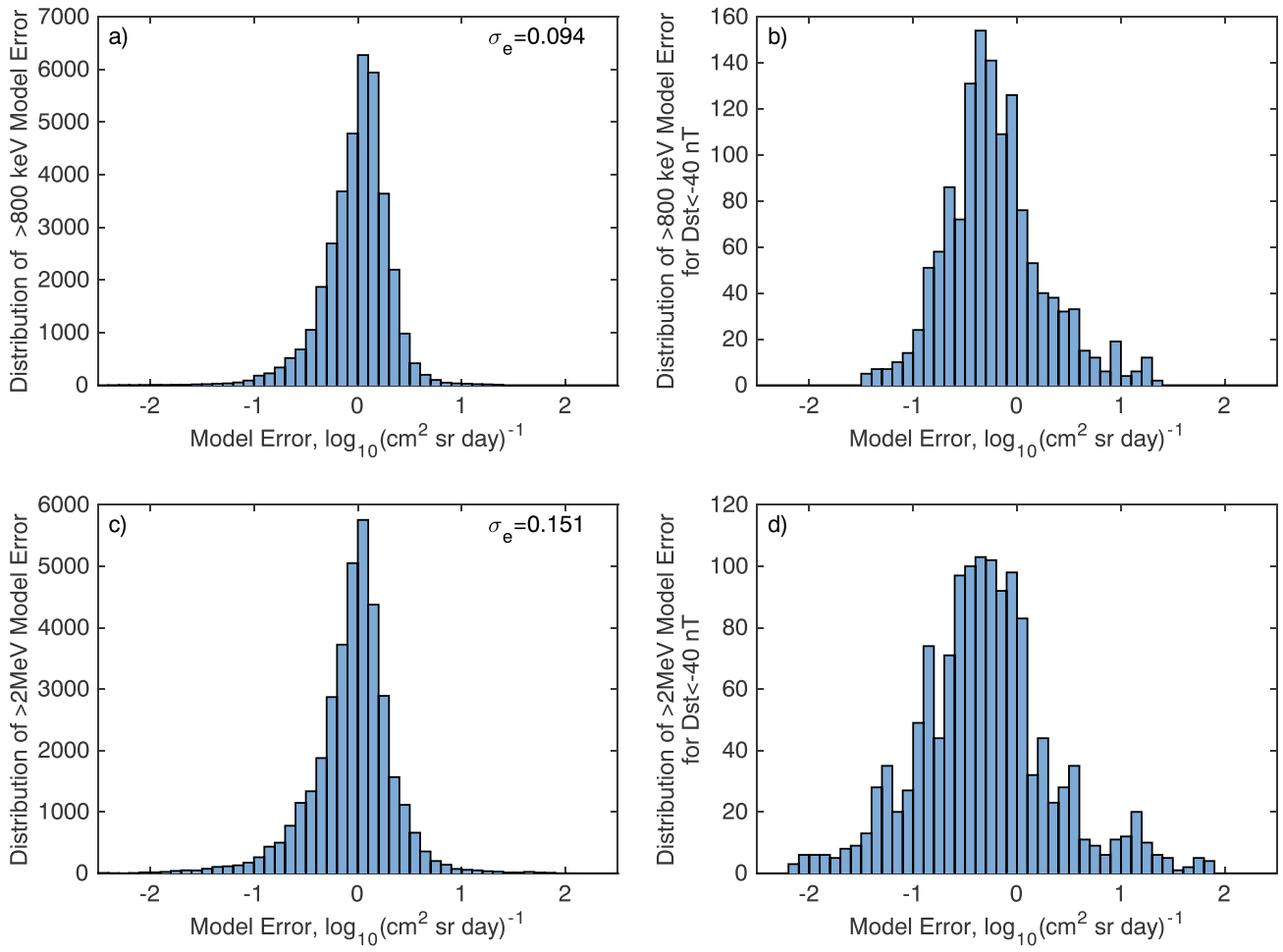

Figure 7. (a and c) Distribution of the model errors ($\log_{10}(J_{GOES}) - \log_{10}(J_{model})$) for the EPS energy channels with the variance of the model errors, σ_e, shown in the top right of each panel. (b and d) Distribution of the model errors when $Dst < -40$ nT.

highest energies peaking a couple of days after, during the storm recovery. This enhancement of the fluxes is forecast by each of the models, with all models increasing within a few hours of the actual onset, some models a few hours before (>2 MeV) and others a few hours after (350–600 keV). Another moderate storm occurs on 1 May 2016 with a *Dst* index of ∼−65 nT. This storm causes a dropout of electron fluxes that recovers the next day for energies >100 keV while causing an enhancement in the two lowest energy channels. The two models for the two lowest energy channels manage to forecast the fluxes accurately; however, the five models that predict fluxes >100 keV do not manage to forecast the dropout. Another dropout occurs on 4 May 2013, during a small storm, for energies >100 keV, while the lower energies had slower decay starting at the same time as the recovery phase of the previous storm on 1 May 2013. Again, the model forecast misses the dropout and so the model error ($e = \log_{10}(J_{GOES}) - \log_{10}(J_{model})$) is negative. This trend is prevalent throughout the data and helps to explain why more large negative errors occur in the distribution (Figures 6 and 7). One of the reasons that the models miss the dropouts in electron fluxes could be due to a faster time scale for the dropouts. The models with energies >100 keV have minimum lags ≥16 h. If the time scales of the dropouts occur quicker than this, then the model will not be able to forecast the dropouts.

If the models fail to predict a dropout or an enhancement, the models tend to lag the output by 24 h. This is due to the past value of election flux term, $J(t - 24)$, within the models. For example, in the case of a missed dropout, the model output will continue as if the sudden change in electron flux has not occurred until after 24 h when the change in the $J(t-24)$ monomial, due to the dropout 24 h earlier, causes the model to decrease. This results in the 24 h delay that can occur with the models.

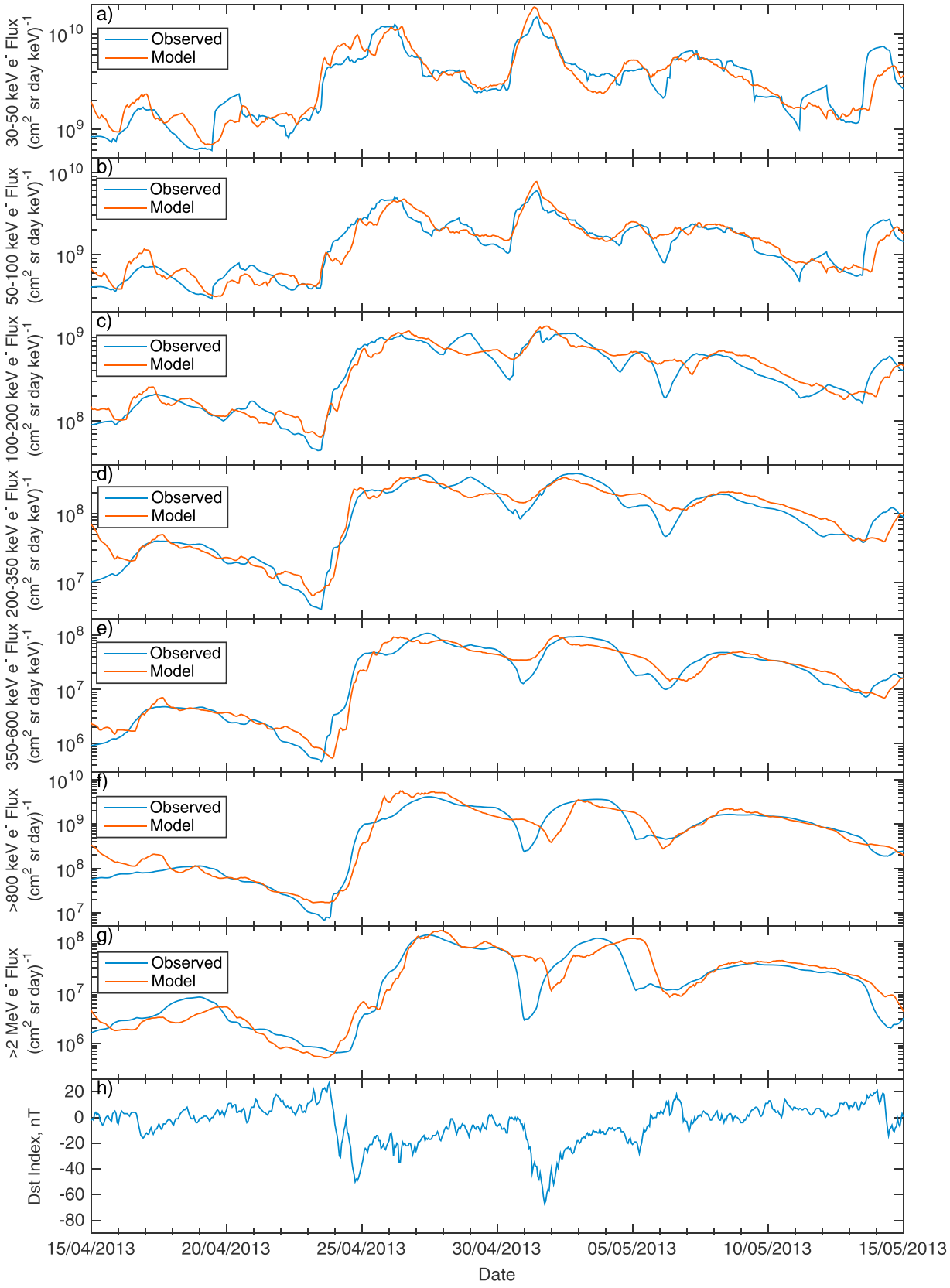

Figure 8. The daily average electron flux measured by GOES in blue and the model forecast in orange for the period from 15 April 2013 to 15 May 2013 (a) 30–50 keV, (b) 50–100 keV, (c) 100–200 keV, (d) 200–350 keV, (e) 350–600 keV, (f) >800 keV, and (g) >2 MeV), with the (h) *Dst* index.

It is worth noting that the convective and substorm-associated electric fields strongly affect the evolution of keV electron fluxes within the inner magnetosphere [*Ganushkina et al.*, 2013, 2014, 2015], leading to flux variations on time scales significantly shorter then 24 h. The Inner Magnetosphere Particle Transport and Acceleration Model can provide a good nowcast of the short time scale variations, but the model is not able to forecast in advance [*Ganushkina et al.*, 2015].

There are other applications of the models in addition to providing forecasts of the electron fluxes. The models could potentially be employed for the prediction of wave intensities. This could be achieved by using the NARMAX electron flux models in combination with models deduced by *Li et al.* [2013] or *Mourenas et al.* [2014], which are able to estimate the wave activity from the dynamics of electron fluxes.

6. Conclusions

The aim of this study was to create forecast models for the electron flux energy ranges observed by the third-generation GOES satellites, which have an increased temporal resolution over the >800 keV and >2 MeV GEO electron flux models that were previously developed [*Boynton et al.*, 2015]. The increase in time resolution provided by the 1 h moving average data allows for a more continuous forecast of the daily average electron flux rather than producing only one forecast for each UTC day. Instead, every hour the online model is able to forecast the electron flux value over the next 24 h. As such, this study has deduced five new 1 h resolution models for the low-energy electrons measured by GOES, ranging in energy from 30 keV to 600 keV and extended the existing >800 keV and >2 MeV GEO electron flux models to forecast at a 1 h resolution. These models had prediction efficiencies between 66.9% and 73.6% for the period between 1 March 2013 and 28 February 2015.

All of these models are implemented in real time to forecast the electron fluxes at GEO and can be found at the University of Sheffield Space Weather website (www.ssg.group.shef.ac.uk/USSW2/UOSSW.html).

Acknowledgments
Solar wind data were obtained from OMNIweb (http://omniweb.gsfc.nasa.gov/ow_min.html), *Dst* index data from the World Data Center for Geomagnetism, Kyoto (http://wdc.kugi.kyoto-u.ac.jp/index.html), and GOES data from the Nation Oceanic and Atmospheric Administration (http://www.ngdc.noaa.gov/stp/satellite/goes/dataaccess.html). This project has received funding from the European Union's Horizon 2020 Research and Innovation Programme under grant agreement 637302 PROGRESS. M. Balikhin and N.Ganushkina thank the International Space Science Institute in Bern, Switzerland, for their support of the international teams on "Analysis of Cluster Inner Magnetosphere Campaign data, in application the dynamics of waves and wave-particle interaction within the outer radiation belt" and "Ring current modeling: Uncommon Assumptions and Common Misconceptions."

References

Baker, D., R. Belian, P. Higbie, R. Klebesadel, and J. Blake (1987), Deep dielectric charging effects due to high-energy electrons in Earth's outer magnetosphere, *J. Electrostat.*, *20*(1), 3–19.

Baker, D. N., R. L. McPherron, T. E. Cayton, and R. W. Klebesadel (1990), Linear prediction filter analysis of relativistic electron properties at 6.6 R_E, *J. Geophys. Res.*, *95*(A9), 15,133–15,140.

Balikhin, M. A., O. M. Boaghe, S. A. Billings, and H. S. C. K. Alleyne (2001), Terrestrial magnetosphere as a nonlinear resonator, *Geophys. Res. Lett.*, *28*(6), 1123–1126.

Balikhin, M. A., R. J. Boynton, S. A. Billings, M. Gedalin, N. Ganushkina, D. Coca, and H. Wei (2010), Data based quest for solar wind-magnetosphere coupling function, *Geophys. Res. Lett.*, *37*, L24107, doi:10.1029/2010GL045733.

Balikhin, M. A., R. J. Boynton, S. N. Walker, J. E. Borovsky, S. A. Billings, and H. L. Wei (2011), Using the NARMAX approach to model the evolution of energetic electrons fluxes at geostationary orbit, *Geophys. Res. Lett.*, *38*, L18105, doi:10.1029/2011GL048980.

Balikhin, M. A., M. Gedalin, G. D. Reeves, R. J. Boynton, and S. A. Billings (2012), Time scaling of the electron flux increase at GEO: The local energy diffusion model vs observations, *J. Geophys. Res.*, *117*, A10208, doi:10.1029/2012JA018114.

Balikhin, M. A., J. V. Rodriguez, R. J. Boynton, S. N. Walker, H. Aryan, D. G. Sibeck, and S. A. Billings (2016), Comparative analysis of NOAA REFM and SNB^{3}GEO tools for the forecast of the fluxes of high-energy electrons at GEO, *Space Weather*, *14*, 22–31, doi:10.1002/2015SW001303.

Beharrell, M. J., and F. Honary (2016), Decoding solar wind-magnetosphere coupling, *Space Weather*, *14*, doi:10.1002/2016SW001467, in press.

Billings, S., M. Korenberg, and S. Chen (1988), Identification of non-linear output affine systems using an orthogonal least-squares algorithm, *Int. J. Syst. Sci.*, *19*, 1559–1568.

Billings, S., S. Chen, and M. Korenberg (1989), Identification of MIMO non-linear systems using a forward-regression orthogonal estimator, *Int. J. Control*, *49*(6), 2157–2189.

Billings, S. A., and H. L. Wei (2008), An adaptive orthogonal search algorithm for model subset selection and non-linear system identification, *Int. J. Control*, *81*(5), 714–724, doi:10.1080/00207170701216311.

Blake, J. B., W. A. Kolasinski, R. W. Fillius, and E. G. Mullen (1992), Injection of electrons and protons with energies of tens of MeV into $L < 3$ on 24 March 1991, *Geophys. Res. Lett.*, *19*(8), 821–824.

Boaghe, O. M., M. A. Balikhin, S. A. Billings, and H. Alleyne (2001), Identification of nonlinear processes in the magnetospheric dynamics and forecasting of Dst index, *J. Geophys. Res.*, *106*(A12), 30,047–30,066.

Boynton, R. J., M. A. Balikhin, S. A. Billings, A. S. Sharma, and O. A. Amariutei (2011a), Data derived NARMAX Dst model, *Ann. Geophys.*, *29*(6), 965–971, doi:10.5194/angeo-29-965-2011.

Boynton, R. J., M. A. Balikhin, S. A. Billings, H. L. Wei, and N. Ganushkina (2011b), Using the NARMAX OLS-ERR algorithm to obtain the most influential coupling functions that affect the evolution of the magnetosphere, *J. Geophys. Res.*, *116*, A05218, doi:10.1029/2010JA015505.

Boynton, R. J., M. A. Balikhin, S. A. Billings, and O. A. Amariutei (2013a), Application of nonlinear autoregressive moving average exogenous input models to Geospace: Advances in understanding and space weather forecasts, *Ann. Geophys.*, *31*(9), 1579–1589.

Boynton, R. J., M. A. Balikhin, S. A. Billings, G. D. Reeves, N. Ganushkina, M. Gedalin, O. A. Amariutei, J. E. Borovsky, and S. N. Walker (2013b), The analysis of electron fluxes at geosynchronous orbit employing a NARMAX approach, *J. Geophys. Res. Space Physics*, *118*, 1500–1513, doi:10.1002/jgra.50192.

Boynton, R. J., M. A. Balikhin, and S. A. Billings (2015), Online NARMAX model for electron fluxes at GEO, *Ann. Geophys.*, *33*(3), 405–411.

Freeman, J. W., T. P. O'Brien, A. A. Chan, and R. A. Wolf (1998), Energetic electrons at geostationary orbit during the November 3–4, 1993 storm: Spatial/temporal morphology, characterization by a power law spectrum and, representation by an artificial neural network, *J. Geophys. Res.*, *103*(A11), 26,251–26,260.

Friedel, R., G. Reeves, and T. Obara (2002), Relativistic electron dynamics in the inner magnetosphere—A review, *J. Atmos. Sol. Terr. Phys.*, *64*(2), 265–282.

Friederich, U., D. Coca, S. A. Billings, and M. Juusola (2009), Data modelling for analysis of adaptive changes in fly photoreceptors, in *Proceedings of the 16th International Conference on Neural Information Processing: Part I*, vol. 5863, edited by C. S. Leung, M. Lee, and J. H. Chan, pp. 34–38, Springer, Berlin.

Ganushkina, N. Y., O. A. Amariutei, Y. Y. Shprits, and M. W. Liemohn (2013), Transport of the plasma sheet electrons to the geostationary distances, *J. Geophys. Res. Space Physics*, *118*, 82–98, doi:10.1029/2012JA017923.

Ganushkina, N. Y., M. W. Liemohn, O. A. Amariutei, and D. Pitchford (2014), Low-energy electrons (5–50 kev) in the inner magnetosphere, *J. Geophys. Res. Space Physics*, *119*, 246–259, doi:10.1002/2013JA019304.

Ganushkina, N. Y., O. A. Amariutei, D. Welling, and D. Heynderickx (2015), Nowcast model for low-energy electrons in the inner magnetosphere, *Space Weather*, *13*, 16–34, doi:10.1002/2014SW001098.

Gubby, R., and J. Evans (2002), Space environment effects and satellite design, *J. Atmos. Sol. Terr. Phys.*, *64*(16), 1723–1733.

Guo, Y., L. Guo, S. Billings, and H.-L. Wei (2014), An iterative orthogonal forward regression algorithm, *Int. J. Syst. Sci.*, *46*(5), 776–789, doi:10.1080/00207721.2014.981237.

Hanser, F. A. (2011), EPS/HEPAD calibration and data handbook, Tech. Rep. GOESN-ENG-048D, Assur. Technol. Corp., Carlisle, Mass.

Horne, R. B., S. A. Glauert, N. P. Meredith, D. Boscher, V. Maget, D. Heynderickx, and D. Pitchford (2013a), Space weather impacts on satellites and forecasting the Earth's electron radiation belts with SPACECAST, *Space Weather*, *11*, 169–186, doi:10.1002/swe.20023.

Horne, R. B., et al. (2013b), Forecasting the Earth's radiation belts and modelling solar energetic particle events: Recent results from SPACECAST, *J. Space Weather Space Clim.*, *3*, A20.

Koons, H. C., and D. J. Gorney (1991), A neural network model of the relativistic electron flux at geosynchronous orbit, *J. Geophys. Res.*, *96*(A4), 5549–5556.

Leontaritis, I. J., and S. A. Billings (1985a), Input-output parametric models for non-linear systems: Part I. Deterministic non-linear systems, *Int. J. Control*, *41*(2), 303–328.

Leontaritis, I. J., and S. A. Billings (1985b), Input-output parametric models for non-linear systems: Part II. Stochastic nonlinear systems, *Int. J. Control*, *41*(2), 329–344.

Li, W., B. Ni, R. M. Thorne, J. Bortnik, J. C. Green, C. A. Kletzing, W. S. Kurth, and G. B. Hospodarsky (2013), Constructing the global distribution of chorus wave intensity using measurements of electrons by the POES satellites and waves by the Van Allen Probes, *Geophys. Res. Lett.*, *40*, 4526–4532, doi:10.1002/grl.50920.

Li, X. (2004), Variations of 0.7–6.0 MeV electrons at geosynchronous orbit as a function of solar wind, *Space Weather*, *2*, S03006, doi:10.1029/2003SW000017.

Ling, A. G., G. P. Ginet, R. V. Hilmer, and K. L. Perry (2010), A neural network-based geosynchronous relativistic electron flux forecasting model, *Space Weather*, *8*, S09003, doi:10.1029/2010SW000576.

Lohmeyer, W., and K. Cahoy (2013), Space weather radiation effects on geostationary satellite solid-state power amplifiers, *Space Weather*, *11*, 476–488, doi:10.1002/swe.20071.

Lohmeyer, W., A. Carlton, F. Wong, M. Bodeau, A. Kennedy, and K. Cahoy (2015), Response of geostationary communications satellite solid-state power amplifiers to high-energy electron fluence, *Space Weather*, *13*, 298–315, doi:10.1002/2014SW001147.

Mao, K. Z., and S. A. Billings (1997), Algorithms for minimal model structure detection in nonlinear dynamic system identification, *Int. J. Control*, *68*(2), 311–330, doi:10.1080/002071797223631.

Mourenas, D., A. V. Artemyev, O. V. Agapitov, V. Krasnoselskikh, and W. Li (2014), Approximate analytical solutions for the trapped electron distribution due to quasi-linear diffusion by whistler mode waves, *J. Geophys. Res. Space Physics*, *119*, 9962–9977, doi:10.1002/2014JA020443.

Mullen, E. G., M. S. Gussenhoven, D. A. Hardy, T. A. Aggson, B. G. Ledley, and E. Whipple (1986), Scatha survey of high-level spacecraft charging in sunlight, *J. Geophys. Res.*, *91*(A2), 1474–1490.

Olsen, R. C. (1983), A threshold effect for spacecraft charging, *J. Geophys. Res.*, *88*(A1), 493–499.

Osthus, D., P. C. Caragea, D. Higdon, S. K. Morley, G. D. Reeves, and B. P. Weaver (2014), Dynamic linear models for forecasting of radiation belt electrons and limitations on physical interpretation of predictive models, *Space Weather*, *12*, 426–446, doi:10.1002/2014SW001057.

Rastatter, L., et al. (2013), Geospace environment modeling 2008–2009 challenge: D_{st} index, *Space Weather*, *11*, 187–205, doi:10.1002/swe.20036.

Reeves, G. D. (1998), Relativistic electrons and magnetic storms: 1992–1995, *Geophys. Res. Lett.*, *25*(11), 1817–1820.

Temerin, M., and X. Li (2006), Dst model for 1995–2002, *J. Geophys. Res.*, *111*, A04221, doi:10.1029/2005JA011257.

Wei, H. L., and S. A. Billings (2006), An efficient nonlinear cardinal B-spline model for high tide forecasts at the Venice Lagoon, *Nonlinear Processes Geophys.*, *13*(5), 577–584.

Wei, H.-L., and S. A. Billings (2008), Model structure selection using an integrated forward orthogonal search algorithm assisted by squared correlation and mutual information, *Int. J. Model. Ident. Control*, *3*, 341–356.

Wei, H. L., S. A. Billings, and M. Balikhin (2004), Prediction of the *Dst* index using multiresolution wavelet models, *J. Geophys. Res.*, *109*, A07212, doi:10.1029/2003JA010332.

Wei, H.-L., S. A. Billings, A. Surjalal Sharma, S. Wing, R. J. Boynton, and S. N. Walker (2011), Forecasting relativistic electron flux using dynamic multiple regression models, *Ann. Geophys.*, *29*(2), 415–420, doi:10.5194/angeo-29-415-2011.

Wrenn, G. L., D. J. Rodgers, and K. A. Ryden (2002), A solar cycle of spacecraft anomalies due to internal charging, *Ann. Geophys.*, *20*(7), 953–956.